IEEE Access
Multidisciplinary | Rapid Review | Open Access Journal

Received September 5, 2019, accepted September 20, 2019, date of publication September 24, 2019,
date of current version October 8, 2019.

Digital Object Identifier 10.1109/ACCESS.2019.2943421

Super Multi-Armed and Segmented Spiral Pattern in a Reaction-Diffusion Model

JIAN GAO AND CHANGGUI GU
Department of Systems Science, University of Shanghai for Science and Technology, Shanghai 200093, China
Corresponding author: Changgui Gu (gu_changgui@163.com)

This work was supported in part by the National Nature Science Foundation of China under Grant 11875042 and Grant 11505114, and in part by the Shanghai project for construction of top disciplines under Grant USST-SYS01.

ABSTRACT The super multi-armed and segmented (SMAS) spiral pattern has been observed in nature, such as sunflower inflorescence, spiral aloe, pine cone, ball cactus and Roman broccoli, which is characterized by several segmented spiral arms sharing the same spiral tip. The mechanism for the emergency of the SMAS spiral pattern has not been found. In this article, we observed the emergence of the SMAS spiral pattern by the simulations of a reaction-diffusion model. Additionally, our theoretical analysis found that the instability of concentrations in spiral arms leads to the emergence of this pattern. This study provides an alternative explanation for the formation of this type of pattern in nature and sheds light on the dynamics of pattern formation.

INDEX TERMS Spiral pattern, reaction-diffusion model, target-like pattern, superstructure.

I. INTRODUCTION

Pattern formation in reaction-diffusion (RD) systems has been suggested to be an underlying mechanism that gives rise to complex patterns in biology [1]–[7]. For example, spiral patterns obtained in modeling simulations, such as a type of segmented spiral patterns [8], [9] and a type of multi-armed spiral patterns [10]–[14], are used to explain the observation of the natural systems both experimentally and theoretically [8], [15]–[18], e.g., chemical reactions [8], [14]–[16], populations of microorganisms [11], [19], [20], gas discharge [21], [22], and fluid convection [13], [23]. Modelling works have found the mechanisms for the generation of these two types of patterns. Segmented spiral patterns result from an interaction between front rippling via a transverse instability and front symmetry breaking by a fast-diffusing inhibitor far from the Hopf-Turing bifurcation [9], and multi-armed spiral patterns are formed due to attraction of single spirals if these spirals rotate in the same direction and their tips are less than one wavelength apart [10], [11], [16]–[18], [21].

In addition to these two patterns, other spiral patterns have also been observed in nature, e.g., sunflower inflorescence, spiral aloe, pine cone, ball cactus and Roman broccoli [24], [25]. The patterns of pine cone, spiral aloe and ball cactus are shown in Fig. 1. In particular, there exist several segmented spiral arms [26], [27] sharing the same spiral tip in each pattern. We call these patterns the super multi-armed and segmented (SMAS) spiral patterns. Although the SMAS spiral patterns share common features with segmented spiral and multi-armed spiral patterns, they are different. For instance, the arms in SMAS spiral patterns are segmented and in multi-armed spiral patterns are not; SMAS spiral patterns are formed spontaneously and multi-armed spiral patterns are usually induced artificially; although the arms of segmented spiral patterns and SMAS spiral patterns are both segmented, segmented spiral patterns can only have one arm due to the instability of the medium. Thus far, the study and understanding of SMAS spiral patterns are very superficial and deficient to date [24]. Understanding the formation of these patterns in the spiral bodies of such living organisms is still a great scientific challenge.

In this article, we desire to rebuild the SMAS spiral pattern and find the mechanisms for the emergence of this pattern through numerical simulations based on a RD model. Our numerical findings show that this type of spiral pattern contains an explicit superstructure and an implicit stationary target-like structure, which can correspond to the spiral patterns found in nature. Our qualitative theoretical analysis reveals that the SMAS spiral pattern results from the instability of concentrations in spiral arms. The rest of the article is organized as follows. Section II introduces the model and methods; in Section III the numerical simulation results are presented, including the reconstruction of SMAS spiral

The associate editor coordinating the review of this manuscript and approving it for publication was Jenny Mahoney.

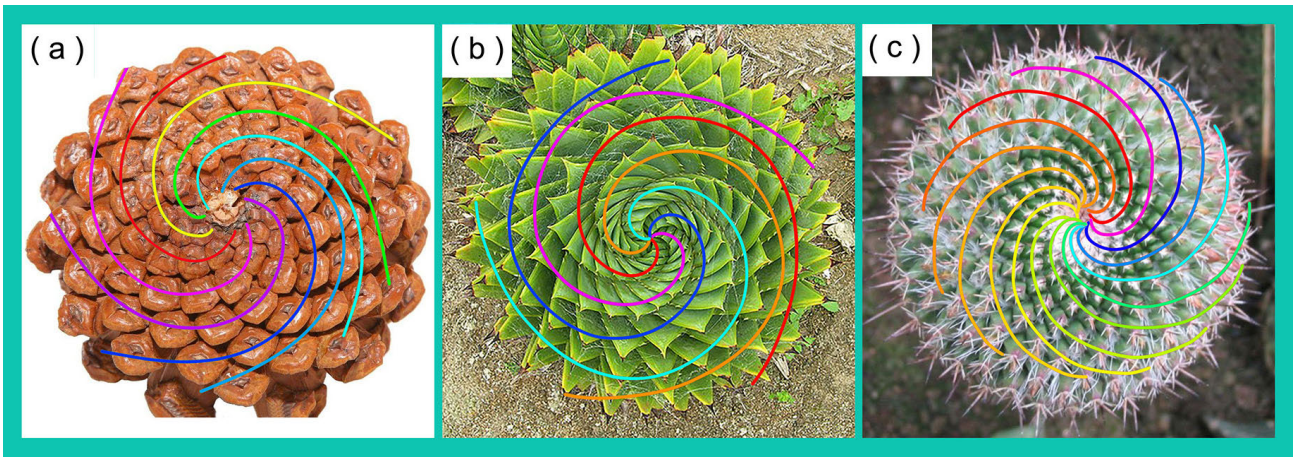

FIGURE 1. (Color online) Examples of the super multi-armed and segmented (SMAS) spiral patterns in living organisms, (a) a pine cone, (b) an spiral aloe, and (c) a ball cactus. The spiral arms in each pattern are marked with solid lines in different colors.

pattern, the composition of the superstructure, the discovery of the stationary target-like structure and so forth; and then, Section IV shows analytical results; at last, discussion and conclusion are presented in Section V.

II. MODEL AND METHOD

The dynamics of spatially distributed systems governed by a modified Decroly-Goldbeter (DG) model [28] are described as below

$$\begin{aligned}\frac{\partial\alpha}{\partial t} &= \frac{\upsilon}{K_{\mathrm{m1}}} - \sigma_1\Phi + D_\alpha\nabla^2\alpha,\\ \frac{\partial\beta}{\partial t} &= q_1\sigma_1\Phi - \sigma_2\eta + D_\beta\nabla^2\beta,\\ \frac{\partial\gamma}{\partial t} &= q_2\sigma_2\eta - k_{\mathrm{s}}\gamma + D_\gamma\nabla^2\gamma,\end{aligned} \tag{1}$$

with

$$\begin{aligned}\Phi &= \frac{\alpha(1+\alpha)(1+\beta)^2}{L_1+(1+\alpha)^2(1+\beta)^2},\\ \eta &= \frac{\beta(1+d\beta)(1+\gamma)^2}{L_2+(1+d\beta)^2(1+\gamma)^2},\end{aligned} \tag{2}$$

where α, β and γ denote the concentrations of reactants S, P_1 and P_2, respectively. Substrate S is injected or synthesized with a constant rate υ; its transformation is catalyzed by an allosteric enzyme, which is activated by its product P_1; a second allosteric enzyme uses P_1 as substrate and is activated by its product P_2; k_{s} is the apparent first-order rate constant after removal of P_2. D_α, D_β and D_γ denote the diffusion coefficient of α, β and γ, respectively. Parameters υ, K_{m1}, σ_1, σ_2, q_1, q_2, L_1, L_2, d, and k_{s} are determined by reaction conditions. Diffusion coefficients of all the three species are set to be equal in this study, i.e, $D_\alpha = D_\beta = D_\gamma$. In the absence of transportation, the above model can show various complex temporal dynamics, including bi-rhythmicity, hard excitation, and chaos when the control parameter k_{s} varies [28]. As in earlier studies [28], [29], k_{s} is investigated as the control parameter in this study. The other parameters are fixed: $\upsilon/K_{\mathrm{m1}} = 0.1\mathrm{s}^{-1}$, $\sigma_1 = \sigma_2 = 10.0\mathrm{s}^{-1}$, $q_1 = 50.0$, $q_2 = 0.02$, $L_1 = 5.0\times10^8$, $L_2 = 100.0$, $d = 1.0\times10^{-6}$, and $D_{\alpha,\beta,\gamma} = 1.00\times10^{-6}\mathrm{cm}^2\cdot\mathrm{s}^{-1}$. The local oscillations in the medium are all single-period limit-cycle oscillations in the investigated range of k_{s} in this article (Movie 1 in the supplementary files describes the motion of a phase point in the phase space which shows a single-period relaxation oscillation).

The solutions for spiral wave pattern in the two-dimensional medium can be expressed as $\Gamma(\rho,\theta,t)$. Here, Γ (a function of space and time) is the spatial distribution of $\gamma_{\rho,\theta}$, where ρ and θ are polar radius and polar angle in the polar coordinates, respectively (The center of the spiral wave is the origin of polar coordinates). $\gamma_{\rho,\theta}$ is the value of γ in the spatial point (ρ, θ). The wave peak is a set of points where $\partial\Gamma(\rho,\theta,t_{\mathrm{x}})/\partial\rho = 0$ and $\Gamma(\rho,\theta,t_{\mathrm{x}}) > \overline{\Gamma}(\rho,\theta,t_{\mathrm{x}})$, where $\overline{\Gamma}(\rho,\theta,t_{\mathrm{x}})$ is the average of all values of γ in all local points when $t = t_{\mathrm{x}}$. Consequently, the maximum values of the system over space and time is defined as following, respectively. $P_{\max}$ is the location of the maximum γ in $\Gamma(\rho,\theta,t_{\mathrm{x}})$ over space, i.e., the position where $\partial\Gamma(\rho,\theta,t_{\mathrm{x}})/\partial\rho = \partial\Gamma(\rho,\theta,t_{\mathrm{x}})/\partial\theta = 0$, $\Gamma(\rho,\theta,t_{\mathrm{x}}) > \overline{\Gamma}(\rho,\theta,t_{\mathrm{x}})$. $\gamma_{\max}$ is the maximum γ of one local point over time, and $\Gamma'(\rho,\theta)$ is the spatial distribution of $\gamma_{\max}$ for all local points. The peak of the target-like structure (target-peak) is a set of points where $\partial\Gamma'(\rho,\theta)/\partial\rho = 0$ and $\Gamma'(\rho,\theta) > \overline{\Gamma'}(\rho,\theta)$, and the valley is a set of points where $\partial\Gamma'(\rho,\theta)/\partial\rho = 0$ and $\Gamma'(\rho,\theta) < \overline{\Gamma'}(\rho,\theta)$, where $\overline{\Gamma'}(\rho,\theta)$ is the average value of the values of $\gamma_{\max}$ for all local points.

For numerical calculation, the partial differential equation (PDE) system (Eq. (1)) was first discretized in space using the *9-point* finite differencing [30]–[33], thus it was reduced to the ordinary differential equation (ODE) system, i.e.,

$$\frac{dx_{\mathrm{m,n}}}{dt} = f(x_{\mathrm{m,n}}) + \frac{D}{h^2}\sum_{\mathrm{i=m-1}}^{\mathrm{m+1}}\sum_{\mathrm{j=n-1}}^{\mathrm{n+1}} M_{\mathrm{i,j}}x_{\mathrm{i,j}}, \tag{3}$$

with

$$\mathbf{M} = \frac{1}{6}\begin{pmatrix} 1 & 4 & 1 \\ 4 & -20 & 4 \\ 1 & 4 & 1 \end{pmatrix}, \tag{4}$$

where x represents the vector of variables α, β and γ, D represents the diffusion coefficient, and $\mathbf{M}$ represents the coupling matrix. The subscripts m and n are the coordinates of gird points. The space step (space grid) is equal to $h = 0.001$cm. Then, the ODE system was carried out by the *4th-order Runge-Kutta* method [30], [34]–[37], which reads

$$\begin{cases} x_{n+1} = x_n + \dfrac{\Delta t}{6}(K_1 + 2K_2 + 2K_3 + K_4), \\ K_1 = f(t_n, x_n), \\ K_2 = f(t_{n+\frac{1}{2}}, x_n + \dfrac{\Delta t}{2}K_1), \\ K_3 = f(t_{n+\frac{1}{2}}, x_n + \dfrac{\Delta t}{2}K_2), \\ K_4 = f(t_{n+1}, x_n + \Delta t K_3), \end{cases} \tag{5}$$

with time steps of $\Delta t = 0.02$s, where $f(t_n, x_n)$ denotes dx_n/dt. The simulations were performed on 1000×1000 grids with *no-flux* boundary conditions. The initial values are selected as $\alpha(1:1000, 1:1000) = 200$, $\beta(1:500, 1:1000) = 1400$, $\beta(501:1000, 1:1000) = 0$, $\gamma(1:1000, 1:500) = 15$, $\beta(1:1000, 501:1000) = 0$.

In order to ensure the reliability of numerical results, the numerical results were also obtained with smaller space steps and time steps. Moreover, the model were also calculated by the *Euler* method, the *4th-order Adams-Bashforth* method and the *4th-order Adams-Bashforth-Moulton* method. Specifically, the *Euler* method [30], [34], [38] reads

$$x_{n+1} = x_n + \Delta t f(t_n, x_n), \tag{6}$$

the *4th-order Adams-Bashforth* method [30], [34], [39], [40] reads

$$x_{n+1} = x_n + \frac{\Delta t}{24}[55f(t_n, x_n) - 59f(t_{n-1}, x_{n-1}) + 37f(t_{n-2}, x_{n-2}) - 9f(t_{n-3}, x_{n-3})], \tag{7}$$

and the *4th-order Adams-Bashforth-Moulton* method [30], [34], [41] reads

$$\begin{cases} \bar{x}_{n+1} = x_n + \dfrac{\Delta t}{24}[55f(t_n, x_n) - 59f(t_{n-1}, x_{n-1}) \\ +37f(t_{n-2}, x_{n-2}) - 9f(t_{n-3}, x_{n-3})], \\ x_{n+1} = x_n + \dfrac{\Delta t}{24}[f(t_{n-2}, x_{n-2}) - 5f(t_{n-1}, x_{n-1}) \\ +19f(t_n, x_n) + 9f(t_{n+1}, \bar{x}_{n+1})]. \end{cases} \tag{8}$$

In this article, the computing programs were written in basic Fortran and MATLAB codes, the figures were drawn by the MATLAB and Origin softwares, the photos in Fig. 1 were taken with a Nikon camera D3200, and the movies were produced by the MATLAB software. Fortran and MATLAB codes to generate the Figures and movies are available from the authors on request.

III. NUMERICAL RESULTS

A. THE RECONSTRUCTION OF SMAS SPIRAL PATTERN

The structure of the spiral wave (snapshot) depends on the value of k_s (Fig. 2). When k_s is less than or equal to the threshold k_s' ($k_s' \approx 0.118\text{s}^{-1}$), a simple and stable spiral wave emerges in the medium (Fig. 2(a)). The concentration in each local point of the wave peak (the white spiral line in the lower panel of Fig. 2(a)) is the same. The spiral tip does not meander, and distances between each two adjacent wave peaks are the same at each moment. Accordingly, the structure of the spiral wave is an Archimedean spiral. When k_s is larger than k_s', the original spiral wave becomes complex and a superstructure appears upon it (Fig. 2(b)). The area of the superstructure extends as k_s continues to increase, until the entire medium is occupied (Fig. 2(c)). The superstructure contains five super arms which are all segmented, and these super arms share the same spiral tip with the original spiral. This superstructure is an SMAS spiral pattern, and we call this type of spiral wave the SMAS spiral wave. Dynamic process of the spiral wave in Fig. 2(c) is tracked in Movie 2 and Movie 3 in the supplementary files. We find that when the superstructure appears, the original spiral wave still retains an Archimedean spiral structure, and the spiral tip still does not meander in Fig. 2(c). Therefore, the plane structure of wave peak of the spiral wave can be represented as

$$\rho(\theta) = \frac{\lambda_S(\theta - \theta_0)}{2\pi}, \tag{9}$$

where λ_S is the wavelength of the spiral ($\approx 58.53 \times 10^{-3}$cm), and ρ ($0 < \rho < +\infty$) and θ ($\theta_0 \leq \theta < +\infty$) are polar coordinates. ρ is a function of θ, and θ_0 ($0 \leq \theta_0 < 2\pi$) is the initial angle. Note that the center of the spiral wave is the origin of polar coordinates.

In the next subsections, we will investigate the typical features for the SMAS spiral wave.

B. THE COMPOSITION OF THE SUPERSTRUCTURE

As shown in Fig. 2(b) and (c), the superstructure is a spacial ordered structure that is formed by areas of higher concentrations in spiral arms, i.e., the maximum concentrations over space in the spiral wave. The locations of the these maximum concentrations over space are denoted as $P_{\max}$. The points ($P_{\max}$) for the three spiral waves from Fig. 2(a), (b) and (c) are marked in Fig. 3(a), (b) and (c), respectively. Note that if we number $P_{\max}$ from the spiral tip along the original spiral arm as positive integers, i.e., $5m + k$, ($m \in N^*, k = -4, -3, -2, -1, 0$), where m denotes the sequence numbers of these points $P_{\max}$ (counted from the spiral tip along the super-spiral), N^* denotes the positive integer, the points $P_{\max}$ can constitute a super-spiral structure for each k. For instance, the points numbered 2, 7, 12, 17, 22, 27, $\cdots$, constitute a super-spiral structure (i.e., the red solid line in Fig. 3(c)). In Fig. 3(c), several selected sequence numbers $P_{\max}$ are marked in the form of (m, k). In general, as shown in Fig. 3(c), all points $P_{\max}$ in the spiral arm form a five-armed super-spiral wave, i.e., the superstructure upon the original

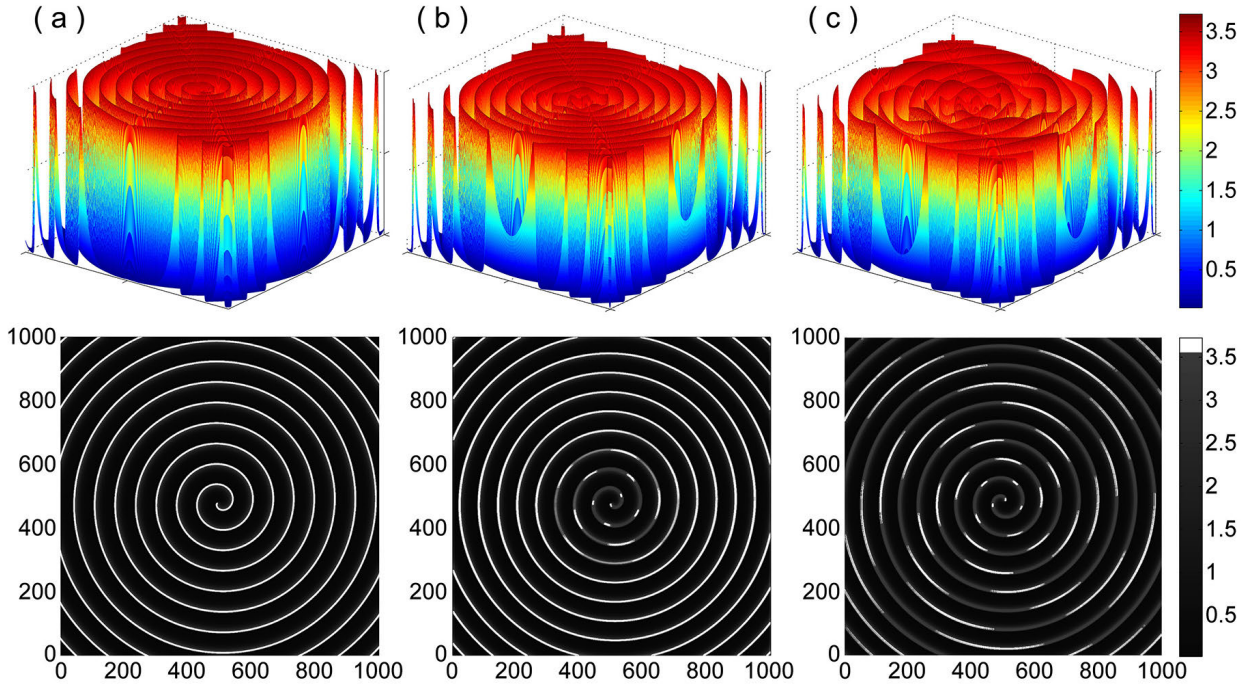

FIGURE 2. (Color online) The spatial distribution of $\gamma_{\rho,\theta}$ when $t = t_x$, i.e., $\Gamma(\rho, \theta, t_x)$, in the medium with selected values of k_s: (a) 0.118s^{-1}, (b) 0.124s^{-1} and (c) 0.128s^{-1}. The figures in the lower part of (a), (b) and (c) are the corresponding plane figures. The movies of the SMAS spiral wave in (c) can be enhanced in Movie 3 in the supplementary files. The spiral waves are snapshots when $t = t_x$, i.e., $\Gamma(\rho, \theta, t_x)$, where t_x represents any moment when spiral waves reach steady states.

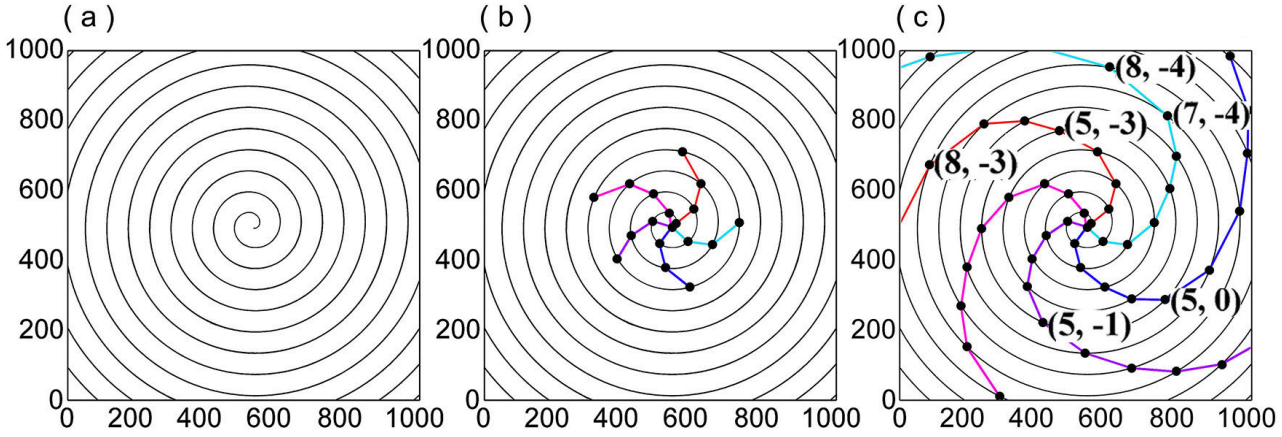

FIGURE 3. (Color online) The spatial distribution of the points P_{max} (labelled by black solid circles) in the spiral wave (black solid line) with different values of k_s: (a) 0.118s^{-1}, (b) 0.124s^{-1} and (c) 0.128s^{-1}. The super arms are marked with solid lines in different colors, respectively. Several selected sequence numbers of P_{max} are marked on the right side of the corresponding points in the form of (m, k), respectively. Note that point P_{max} does not exist in (a).

spiral wave shown in Fig. 2(c). The structure of these five super arms are identical.

C. THE DISCOVERY OF STATIONARY TARGET-LIKE STRUCTURE

In the three spiral waves in Fig. 2, we recorded maximal concentrations γ_{max} over time for each local point (Fig. 4). Results show that the concentrations γ_{max} for each local point in Fig. 2(a) are the same except the points near the spiral core (Fig. 4(a)). When the superstructure occurs (Fig. 2(b)), a stationary target-like structure appears at the center of $\Gamma'(\rho, \theta)$ (Fig. 4(b)). As shown in the appended drawing in Fig. 4(b), with the increase of ρ, the amplitudes of oscillations of the wavy line (i.e., the change in concentration in the target-like pattern along the radial direction) gradually decrease and subside to a certain value of ρ. The superstructure occupies the same area as the target-like structure. As k_s increases, the superstructure expands synchronously with the target-like

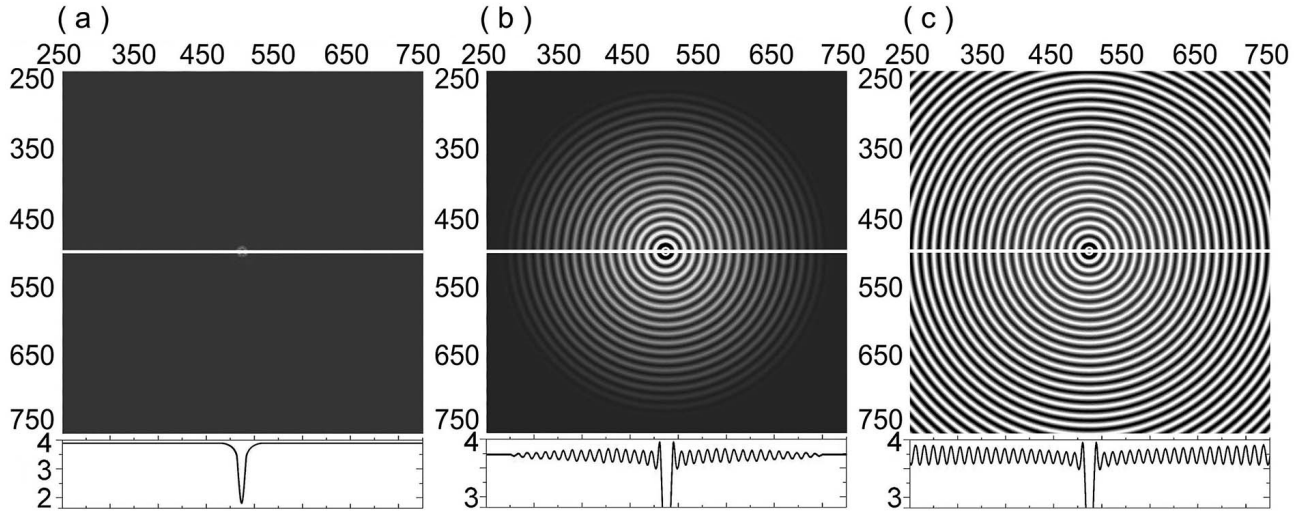

FIGURE 4. The spatial distribution of γ_{max}, i.e., $\Gamma'(\rho, \theta)$, in the medium with different values of k_s: (a) $0.118s^{-1}$, (b) $0.124s^{-1}$ and (c) $0.128s^{-1}$. The appended drawings below (a), (b) and (c) are the longitudinal sections (along the white solid lines) of the corresponding $\Gamma'(\rho, \theta)$, respectively. (a), (b) and (c) all show a part of the total medium.

structure, finally the target-like structure occupies the whole medium (Fig. 4(c)). The peak of this target-like structure can be represented as

$$\rho(n) = n\lambda_T, \quad (n \in N), \tag{10}$$

where n denotes the sequence numbers (counted from the center) of the circles, polar coordinate of the spatial points ρ ($0 < \rho < +\infty$) is a function of n, and N denotes the natural number.

To explain the formation of the target-like pattern, we have randomly selected a wave in Fig. 2(c), and studied its propagation characteristic. Results show that the wave peak is swinging up and down during the propagation process (Movie 4 in the supplementary files describes the dynamic process of the wave peak). Moreover, the trajectory of the wave peak is the same as the wavy line in the appended drawing of Fig. 4(c). The trajectories of the wave peaks having the same propagating direction can overlap with each other. Thus the trajectories of all wave peaks could form a surface, i.e., the target-like pattern in Fig. 4(c).

D. NUMERICAL RESULTS OBTAINED WITH SMALLER SPACE STEPS AND TIME STEPS

In order to ensure the reliability of numerical results, the model was also calculated by the *4th-order Runge-Kutta* method when the space and time steps are reduced to half of the original values, i.e., the space step h is equal to 0.0005cm and the time step Δt is equal to 0.01s. Note that, to keep the spatial scale of the medium unchanged, the simulations were performed on 2000×2000 grids. Because what we need to verify is the reliability of the superstructure of the SMAS spiral wave, the control parameter k_s is fixed at $0.128s^{-1}$.

Figure 5 shows corresponding numerical results. By comparing Fig. 2(c) and Fig. 5(a), Fig. 4(c) and Fig. 5(b), we found that the numerical results are the same when the space and time steps are reduced to half of the original values. In order to quantify the comparison of these two numerical results, i.e., the SMAS spiral waves in Fig. 2(c) and Fig. 5(a), we have found out the locations of all the maxima in the spiral waves at a certain moment, i.e., the P_{max} points. The spiral arms of the two spiral waves can be perfectly overlapped, which are denoted as the black spiral line in Fig. 5(c). Figure 5(c) shows the P_{max} points in Fig. 2(c) and Fig. 5(a). One can find that the corresponding points are highly consistent.

E. NUMERICAL RESULTS OBTAINED BY OTHER NUMERICAL METHODS

To further ensure the correctness and reliability of the numerical results, we have re-simulated the model with three other algorithms, i.e., the *Euler* method, the *4th-order Adams-Bashforth* method and the *4th-order Adams-Bashforth-Moulton* method,respectively. The space steps and time steps used here are 0.001cm and 0.02s, which are the same as in MODEL AND METHOD section, and the simulations are also performed on 1000×1000 grids. The control parameter k_s is fixed as $0.128s^{-1}$ to verify the reliability of the superstructure of the SMAS spiral wave.

Figure 6 shows the SMAS spiral waves and the corresponding target-like patterns (The drawing below each panel is the corresponding target-like pattern). The SMAS spiral waves in (a), (b) and (c) are obtained by the *Euler*, the *4th-order Adams-Bashforth* and the *4th-order Adams-Bashforth-Moulton* methods, respectively. One can find that the numerical results from different algorithms are all the SMAS spiral waves.

The SMAS spiral waves from different algorithms are then compared quantitatively. All the P_{max} points of the three

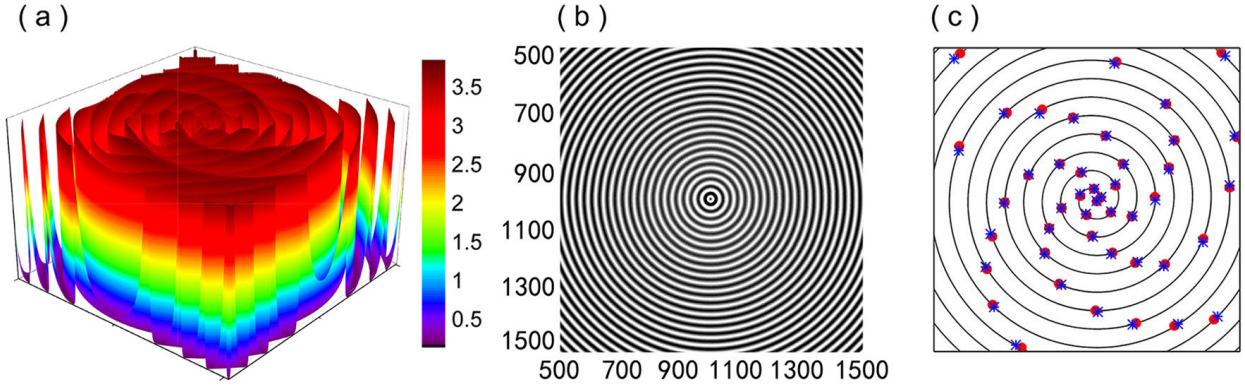

FIGURE 5. (Color online) The simulation results obtained with smaller space steps and time steps: (a) the SMAS spiral wave (the spatial distribution of $\gamma_{\rho,\theta}$); (b) the target-like pattern (the spatial distribution of $\gamma_{\max}$); (c) the comparisons between the corresponding $P_{\max}$ points in Fig. 2(c) and Fig. 5(a). The black spiral line indicates the spiral peaks of the spiral waves in Fig. 2(c) and Fig. 5(a). In (c), the solid red circles represents $P_{\max}$ points in Fig. 2(c), and the blue stars indicates $P_{\max}$ points in Fig. 5(a).

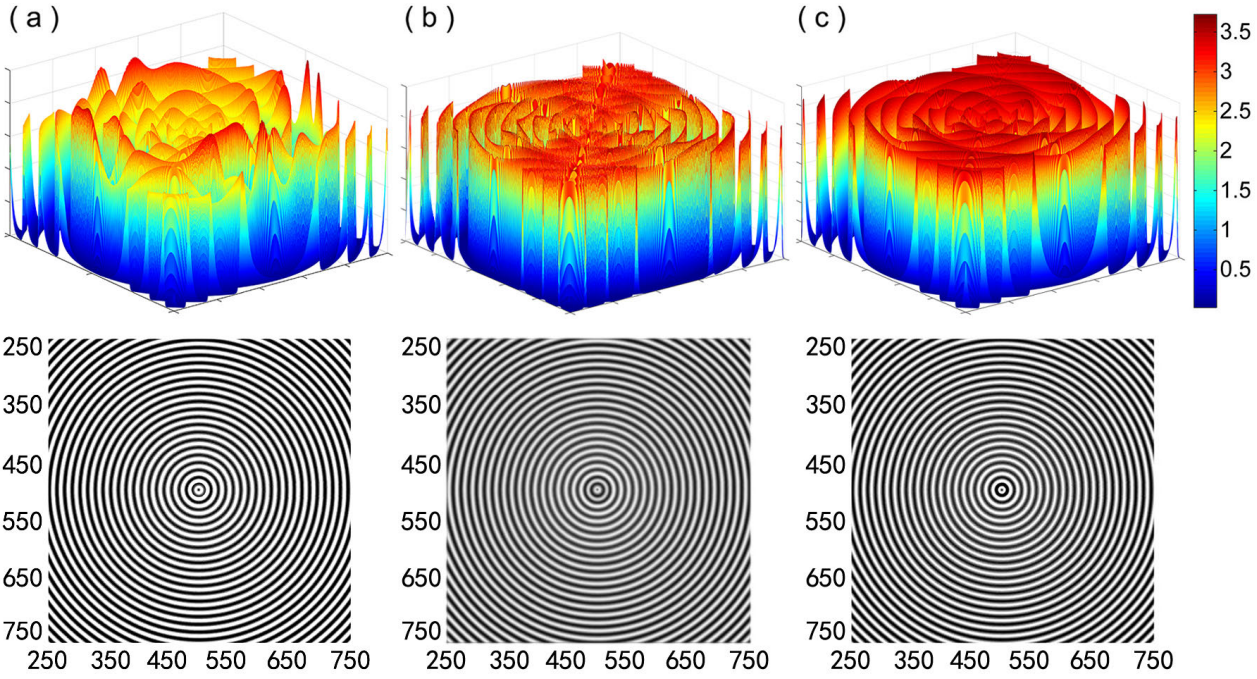

FIGURE 6. (Color online) Numerical results obtained by different numerical methods. The simulation results in (a), (b) and (c) are obtained by the *Euler*, the *4th-order Adams-Bashforth* and the *4th-order Adams-Bashforth-Moulton* methods, respectively. The spiral wave (the spatial distribution of $\gamma_{\rho,\theta}$) is shown as elevation in the upper panel in each figure, and the target-like pattern (the spatial distribution of $\gamma_{\max}$) is shown in the lower panel.

SMAS spiral waves in Fig. 6 are found and marked with different symbols (Fig. 7). The spiral arms of the three spiral waves can be perfectly overlapped, which are denoted as the black spiral line in Fig. 7. Consequently, the results in Fig. 7 illustrate the high degree of agreement between the results obtained by different algorithms. It is also proved that the superstructure of the SMAS spiral wave is not caused by the limitation of a certain algorithm.

IV. ANALYTICAL RESULTS

Our simulations show that, when k_s increases, the target-like structure and superstructure appear simultaneously, expand synchronously and occupy the same area in Fig. 4. These indicate that the superstructure of SMAS spiral waves may be due to the emergence of the target-like structure. To prove the conjecture, by utilizing Eq. (2) and Eq. (3), we calculate the coordinates of intersection points of the peak of the spiral wave (described by Eq. (2)) and the peak of the target-like structure (described by Eq. (3)), i.e., $(n\lambda_T,\ 2n\pi\lambda_T/\lambda_S + \theta_0),\ n \in N$. The appropriate situations of these coordinates are exactly $P_{\max}$. The theoretical analysis is consistent with the simulation result.

By analyzing the relationship between these coordinates, we find that $\zeta \equiv \lambda_S/\lambda_T$ is the key factor which affects

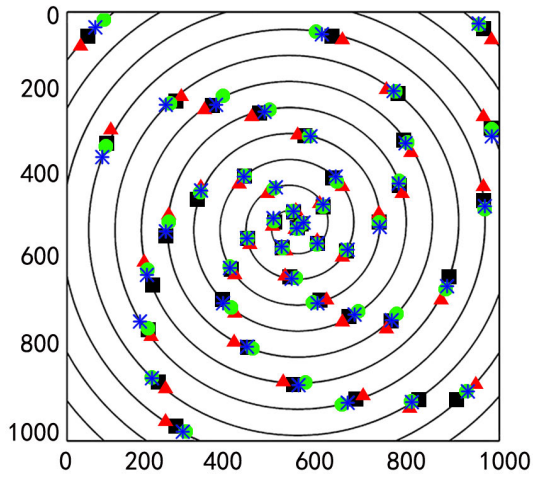

FIGURE 7. The comparisons between the corresponding P_{max} points in Fig. 6(a), (b) and (c). The black spiral line indicates the spiral peaks of the spiral waves in Fig. 6(a), (b) and (c). The black squares, red triangles, green circles and blue stars represents P_{max} points in Fig. 2(c), Fig. 6(a), (b) and (c), respectively.

the superstructure. We set $\zeta = j + \xi$, $j \in N^*$, $-0.5 < \xi \leq 0.5$, then $(n\lambda_T,\ 2n\pi\lambda_T/\lambda_S + \theta_0)$ is expressed as $(n\lambda_T,\ 2\pi n/(j+\xi) + \theta_0)$. As shown in Fig. 3(c), each super arm is formed by the points P_{max} (intersections) of the nearest polar angle between adjacent intersections. Thus, a group of intersections having the polar angles $2\pi[0/(j+x)] + \theta_0$, $2\pi[j/(j+\xi)] + \theta_0$, $2\pi[2j/(j+\xi)] + \theta_0$, $2\pi[3j/(j+\xi)] + \theta_0$, $\cdots$, form a super arm. Because the increments of polar radius and polar angle between adjacent intersections in this group are both equal, i.e., polar radius is proportional to polar angle, this super arm is an Archimedean spiral. These intersections can be divided into j groups whose starting points' polar angles are $2\pi[0/j+\xi)] + \theta_0$, $2\pi[1/(j+\xi)] + \theta_0$, $2\pi[2/(j+\xi)] + \theta_0$, $2\pi[3/(j+\xi)] + \theta_0, \cdots, 2\pi[j-1/(j+\xi)] + \theta_0$, respectively. Moveover, the value of ξ affects the chirality of the super arm. When ξ is less than 0, the increment of polar angle between adjacent intersections in one group is greater than zero, i.e., $2\pi[j/(j+\xi)] > 0$, thus the chirality of the super arm is the same to the original spiral wave's. In the same way, when ξ is great than 0, the chirality of the super arm is opposite to the original spiral wave's. Especially, when ξ is equal to 0, the super arms are straight, and when ξ is equal to 0.5, it is difficult to distinguish the super arms. For instance, in Fig. 2(c), with $\zeta \approx 4.71$, the superstructure has 5 super arms, the chirality of the super arm is the same to the original spiral wave's. In Fig. 8(a), with $\zeta \approx 3.32$, the superstructure has 3 super arms, the chirality of the super arm is opposite to the original spiral wave's. Movie 5 in the supplementary files shows the simulation process of a superposition of an Archimedean spiral and a target ring. Analytical results are coherent with simulation results in Movie 5.

In order to explain the formation mechanism of SMAS spiral waves, we simplify the DG model and study SMAS spiral waves combining with Fig. 2-4. Because the changes of α are very small relative to its average level in the reaction process [28], we let α to be constant, therefore, Eq. (1) can be simplified as a bivariate model. Moreover, the model was further simplified, which reads

$$\begin{aligned} \frac{\partial \beta}{\partial t} &= q_1\sigma_1\Phi' - \sigma_2\eta' + D_\beta\nabla^2\beta, \\ \frac{\partial \gamma}{\partial t} &= q_2\sigma_2\eta' - k_s\gamma + D_\gamma\nabla^2\gamma, \end{aligned} \tag{11}$$

with

$$\begin{aligned} \Phi' &= \frac{A\beta^2}{L_1 + B\beta^2}, \\ \eta' &= \frac{\beta\gamma^2}{L_2}. \end{aligned} \tag{12}$$

Analyses indicate that this simplified model is an excitable system, and β is the activator variable. Indeed, in the original

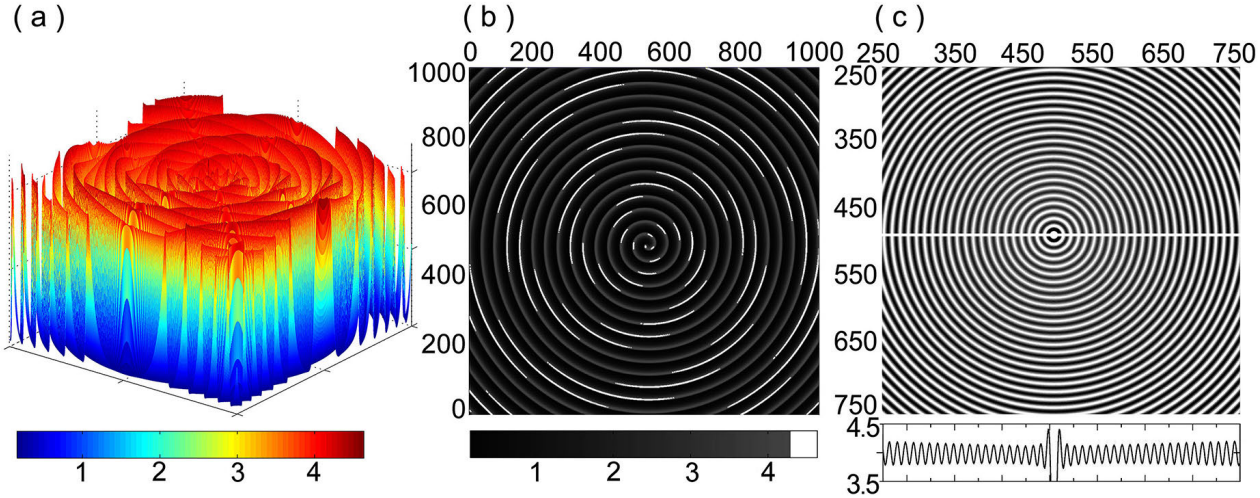

FIGURE 8. (Color online) The simulation results of Eq. 11. (a) the spatial distribution of $\gamma_{\rho,\theta}$, i.e., $\Gamma(\rho,\theta,t_x)$, (b) the corresponding plane figure of (a), (c) $\Gamma'(\rho,\theta)$ in the spiral wave in (a). The parameters are $A = 6500.0\text{nM}^2$, $B = 8800.0\text{nM}^2$, and $k_s = 0.128\text{s}^{-1}$.

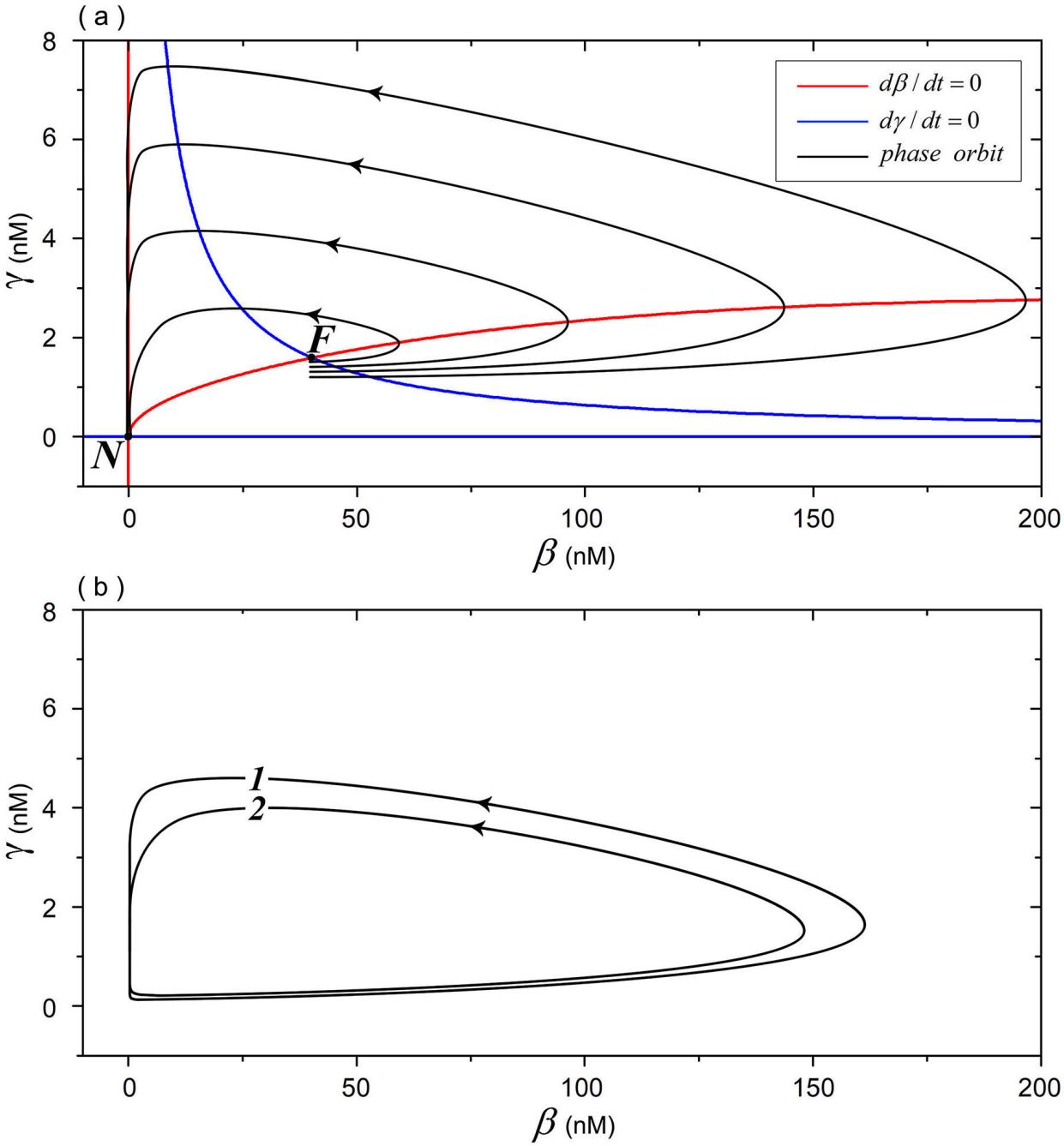

FIGURE 9. (Color online) (a) The phase diagram of Eq. 11 in a homogeneous phase medium. The red solid lines are the graph of equation $d\beta/dt = 0$, the blue solid lines are the graph of equation $d\gamma/dt = 0$, the black solid lines are phase orbits. The black arrows indicate the directions of trajectories. Point F is the intersection of the red and blue lines, i.e. the fixed points. The starting points of the trajectories are very close to each other. (b) Two typical phase orbits of the local points in the SMAS spiral wave in Fig. 8.

DG model, the homogeneous oscillation is a relaxation oscillation, which is a typical characteristic for excitatable systems. Accordingly, the DG model possesses the characteristic of excitatable systems.

We also obtain the SMAS spiral wave in this simplified model (Fig. 8(a,b)). The spatial distribution of $\gamma_{\max}$, i.e., $\Gamma'(\rho, \theta)$, shows a target-like pattern as well (Fig. 8(c)). One can find that the number of the super arm in Fig. 2(c) is 5 and in Fig. 8(a) is 3, because the value of ζ in Fig. 2(c) is 4.71 and in Fig. 8(a) is 3.32. Because the characteristics of spiral waves in RD systems largely depends on reaction terms, and not on diffusion terms [42]–[46], we study the formation mechanism of the special mode of propagation of waves by analyzing the dynamical behavior of a single oscillator.

Two fixed points of Eq. (11), points N and F, are obtained (Fig. 9(a)). The analysis of stability shows that point N (the coordinate origin) is a stable nodal point, stable along the γ axis, neutral along the β axis. This neutrality leads the excitation threshold to be zero. Point F is an unstable focal point. The red and blue solid lines are the nullclines of β and γ, respectively. Several phase orbits are drawn, with the arrows denoting the directions of the trajectories (Fig. 9(a)). The phase points, which are very close to each other at the initial time, will go away from each other, and the maximum values of β or γ to be achieved will be quite different. This indicates that the system is very sensitive to the initial value of γ which is affected by the excitation condition. An small perturbation can have a huge effect on the result. Figure 9(b) shows two typical phase-orbits in the medium supporting spiral waves. Orbits 1 and 2 are the phase orbits of local points at the target peak and valley in the target-like structure in Fig. 8(b), respectively. In fact, there are countless orbits (undrawn) between these two orbits, which are the phase orbits of points between the target peak and valley in Fig. 8(b). This feature of the orbits is consistent with the results of the original model. The difference between orbits 1 and 2 in Fig. 9(b) is caused by their excitation conditions.

For convenient analysis, we disperse the spatial excitation progress (i.e., the propagation process of the wave) to an iterative process. In this paper, we study the evolution between two waves of different concentrations in an iterative way, and use the concentration of wave peak to represent the concentration of the wave. In Fig. 9(a), we can obtain that the maximum β of the i_{th} wave (denoted as $\beta_{\text{max,i}}$) to be achieved has a negative correlation with the initial γ (denoted as $\gamma_{\text{init,i}}$), i.e.,

$$\beta_{\text{max,i}} \propto \frac{1}{\gamma_{\text{init,i}}},$$

where i means the i_{th} generation. $\beta_{\text{max,i}}$ has a positive correlation with the maximum γ (denoted as $\gamma_{\text{max,i}}$), i.e.,

$$\beta_{\text{max,i}} \propto \gamma_{\text{max,i}}.$$

Moreover, $\gamma_{\text{init,i}}$ is positively correlated with γ in excitation conditions. Since the excitation is caused by the diffusion process, and the intensity of the diffusion is related to the concentration gradient, the peak of the $(i-1)_{\text{th}}$ wave has a greater contribution to the excitation of the i_{th} wave. Therefore, we roughly consider $\gamma_{\text{max,i}-1}$ to be γ in the excitation condition. We can obtain

$$\gamma_{\text{init,i}} \propto \gamma_{\text{max,i}-1}.$$

Finally, we can derive that

$$\beta_{\text{max,i}} \propto \frac{1}{\beta_{\text{max,i}-1}},$$

and

$$\gamma_{\text{max,i}} \propto \frac{1}{\gamma_{\text{max,i}-1}},$$

i.e., the concentration of the i_{th} wave is negatively related to the concentration of the last generation wave. Therefore, the wave peak will be swinging up and down during the propagation process. This phenomenon is a cyclical change, thus we can obtain these target-like structures in Fig. 4 and Fig. 8(c). Finally, we observed the superstructure in Fig. 2(c) and Fig. 8(a).

We find that the negative correlation between adjacent two generation waves is due to the structure of the nullclines in the phase space. In a general excitable medium supporting spiral waves, such as FitzHugh-Nagumo model, the phase orbits of local oscillations are the same except those near the spiral tip. The nullcline of the trigger variable always has a shape of an 'inverted N' or a 'lain S' [47]–[49], which prevents the increase of the trigger variable. Therefore, the trigger variable has a fixed maximum value. However, in this simplified model, the nullcline of trigger variable does not tilt downward, and its slope is not less than zero. Therefore, the nullcline can not prevent the increase of trigger variable in time, which leads to the instability of waves. It is a type of instability that waves oscillate up and down during the propagation process. In summary, SMAS spiral waves are caused by the instability of concentrations in spiral arms.

V. DISCUSSION AND CONCLUSION

In the present article, a type of spiral wave, i.e., SMAS spiral wave, has been studied, which exists in nature. The SMAS spiral wave has been rebuilt through our numerical simulation methods. Moreover, we have found that the SMAS spiral wave is caused by the instability of concentrations in spiral arms. The structure and formation mechanism of the SMAS spiral wave are different from other complex spiral waves. For other spiral waves, Ref. [50] pointed out that the formations of complex spiral waves from simple ones are accompanied by the transition of the local oscillations from simple oscillation to complex oscillation. However, when the SMAS spiral wave appears, the local oscillation is still simple. Additionally, in all spiral waves previously discovered, all the maximum values for local points are equal except those near the spiral tip, whereas in the SMAS spiral wave, the maximum values for local points are not equal and the spatial distribution of these maximum values has a stationary target-like structure. At last, the target-like structure in Fig. 4(c) is a special phenomenon. Our findings not only alternatively explain the formation mechanism of the SMAS spiral pattern in nature, but also enrich the theory research of the pattern formation.

REFERENCES

[1] A. M. Turing, "The chemical basis of morphogenesis," *Phil. Trans. Roy. Soc. B*, vol. 237, pp. 37–72, Aug. 1952.

[2] T. E. Woolley, R. E. Baker, P. K. Maini, J. L. Aragón, and R. A. Barrio, "Analysis of stationary droplets in a generic turing reaction-diffusion system," *Phys. Rev. E, Stat. Phys. Plasmas Fluids Relat. Interdiscip. Top.*, vol. 82, no. 5, 2010, Art. no. 051929.

[3] M. Baurmann, W. Ebenhöh, and U. Feudel, "Turing instabilities and pattern formation in a benthic nutrient-microorganism system," *Math. Biosci. Eng.*, vol. 1, no. 1, pp. 111–130, 2004.
[4] J. Wang, J. Wei, and J. Shi, "Global bifurcation analysis and pattern formation in homogeneous diffusive predator–prey systems," *J. Differ. Equ.*, vol. 260, pp. 3495–3523, Feb. 2016.
[5] J. Wang, J. Shi, and J. Wei, "Dynamics and pattern formation in a diffusive predator–prey system with strong Allee effect in prey," *J. Differ. Equ.*, vol. 251, pp. 1276–1304, Aug. 2011.
[6] J. R. Potts and M. A. Lewis, "How memory of direct animal interactions can lead to territorial pattern formation," *J. Roy. Soc. Interface*, vol. 13, no. 118, 2016, Art. no. 20160059.
[7] R. L. Cooper, A. P. Thiery, A. G. Fletcher, D. J. Delbarre, L. J. Rasch, and G. J. Fraser, "An ancient turing-like patterning mechanism regulates skin denticle development in sharks," *Sci. Adv.*, vol. 4, no. 11, 2018, Art. no. eaau5484.
[8] V. K. Vanag and I. R. Epstein, "Segmented spiral waves in a reaction-diffusion system," *Proc. Nat. Acad. Sci. USA*, vol. 100, no. 25, pp. 14635–14638, 2003.
[9] L. Yang, I. Berenstein, and I. R. Epstein, "Segmented waves from a spatiotemporal transverse wave instability," *Phys. Rev. Lett.*, vol. 95, Jul. 2005, Art. no. 038303.
[10] E. A. Ermakova, A. M. Pertsov, and E. E. Shnol, "On the interaction of vortices in two-dimensional active media," *Phys. D, Nonlinear Phenomena*, vol. 40, pp. 185–195, Dec. 1989.
[11] B. Vasiev, F. Siegert, and C. Weijer, "Multiarmed spirals in excitable media," *Phys. Rev. Lett.*, vol. 78, pp. 2489–2492, Mar. 1997.
[12] R. M. Zaritski and A. M. Pertsov, "Stable spiral structures and their interaction in two-dimensional excitable media," *Phys. Rev. E, Stat. Phys. Plasmas Fluids Relat. Interdiscip. Top.*, vol. 66, Dec. 2002, Art. no. 066120.
[13] S. V. Kiyashko, L. N. Korzinov, M. I. Rabinovich, and L. S. Tsimring, "Rotating spirals in a Faraday experiment," *Phys. Rev. E, Stat. Phys. Plasmas Fluids Relat. Interdiscip. Top.*, vol. 54, pp. 5037–5040, Nov. 1996.
[14] K. I. Agladze and V. I. Krinsky, "Multi-armed vortices in an active chemical medium," *Nature*, vol. 296, pp. 424–426, Apr. 1982.
[15] V. I. Krinsky and K. I. Agladze, "Interaction of rotating waves in an active chemical medium," *Phys. D, Nonlinear Phenomena*, vol. 8, pp. 50–56, Jul. 1983.
[16] O. Steinbock and S. C. Müller, "Light-controlled anchoring of meandering spiral waves," *Phys. Rev. E, Stat. Phys. Plasmas Fluids Relat. Interdiscip. Top.*, vol. 47, p. 1506, Mar. 1993.
[17] M. Ruiz-Villarreal and M. Gómez-Gesteira, C. Souto, A. P. Muñuzuri, and V. Pérez-Villar, "Long-term vortex interaction in active media," *Phys. Rev. E, Stat. Phys. Plasmas Fluids Relat. Interdiscip. Top.*, vol. 54, pp. 2999–3002, Sep. 1996.
[18] I. Schebesch and H. Engel, "Interacting spiral waves in the oregonator model of the light-sensitive Belousov-Zhabotinskii reaction," *Phys. Rev. E, Stat. Phys. Plasmas Fluids Relat. Interdiscip. Top.*, vol. 60, pp. 6429–6434, Dec. 1999.
[19] K. J. Lee, E. C. Cox, and R. E. Goldstein, "Competing patterns of signaling activity in *Dictyostelium* discoideum," *Phys. Rev. Lett.*, vol. 76, no. 7, p. 1174, 1996.
[20] C. van Oss, A. V. Panfilov, P. Hogeweg, F. Siegert, and C. J. Weijer, "Spatial pattern formation during aggregation of the slime moulddictyostelium discoideum," *J. Theor. Biol.*, vol. 181, pp. 203–213, Aug. 1996.
[21] L. Dong, H. Wang, F. Liu, and Y. He, "Core dynamics of a multi-armed spiral pattern in a dielectric barrier discharge," *New J. Phys.*, vol. 9, no. 9, p. 330, 2007.
[22] L. Dong, F. Liu, S. Liu, Y. He, and W. Fan, "Observation of spiral pattern and spiral defect chaos in dielectric barrier discharge in argon/air at atmospheric pressure," *Phys. Rev. E, Stat. Phys. Plasmas Fluids Relat. Interdiscip. Top.*, vol. 72, Oct. 2005, Art. no. 046215.
[23] E. Bodenschatz, J. R. de Bruyn, G. Ahlers, and D. S. Cannell, "Transitions between patterns in thermal convection," *Phys. Rev. Lett.*, vol. 67, pp. 3078–3081, Nov. 1991.
[24] P. Ball, *The Self-Made Tapestry: Pattern Formation in Nature*. Oxford, U.K.: Oxford Univ. Press, 2001.
[25] D. W. Thompson, *On Growth and Form*. Cambridge, U.K.: Cambridge Univ. Press, 2014.
[26] D. M. Considine and G. D. Considine, *Van Nostrand's Scientific Encyclopedia*. Princeton, NJ, USA: Princeton Univ. Press, 2005.
[27] C. Fumeaux, D. Baumann, and R. Vahldieck, "Finite-volume time-domain analysis of a cavity-backed Archimedean spiral antenna," *IEEE Trans. Antennas Propag.*, vol. 54, no. 3, pp. 844–851, Mar. 2006.
[28] O. Decroly and A. Goldbeter, "Birhythmicity, chaos, and other patterns of temporal self-organization in a multiply regulated biochemical system," *Proc. Nat. Acad. Sci. USA*, vol. 79, no. 22, pp. 6917–6921, 1982.
[29] L. Zhang, Q. Gao, Q. Wang, H. Wang, and J. Wang, "Spiral turbulence developed through the formation of superimposed target waves in an oscillatory reaction-diffusion medium," *Phys. Rev. E, Stat. Phys. Plasmas Fluids Relat. Interdiscip. Top.*, vol. 74, Oct. 2006, Art. no. 046112.
[30] R. D. Richtmyer, *Difference Methods for Initial-Value Problems*. New York, NY, USA: Interscience Publishers, 1957.
[31] C.-H. Jo, C. Shin, and J. H. Suh, "An optimal 9-point, finite-difference, frequency-space, 2-D scalar wave extrapolator," *Geophysics*, vol. 61, no. 2, pp. 529–537, 1996.
[32] T. Potempa, "An improved implementation of the McCracken and Yanosik nine point finite difference procedure," *Appl. Numer. Math.*, vol. 1, pp. 261–272, May 1985.
[33] A. Adigüzel, "New properties of 9-point finite difference solution of the laplace equation" *Medit. J. Math.*, vol. 8, pp. 451–462, Sep. 2011.
[34] J. D. Lambert, *Computational Methods in Ordinary Differential Equations*. New York, NY, USA: Wiley, 1973.
[35] M. L. Johnson, *Essential Numerical Computer Methods*. Beijing, China: Science Press, 2012.
[36] D. J. Evans, "A new 4th order Runge-Kutta method for initial value problems with error control," *Int. J. Comput. Math.*, vol. 39, nos. 3–4, pp. 217–227, 1991.
[37] H. Musa, I. Saidu, and M. Y. Waziri, "A simplified derivation and analysis of fourth order Runge Kutta method," *Int. J. Comput. Appl.*, vol. 9, no. 8, pp. 51–55, 2010.
[38] J. Jacod and P. Protter, "Asymptotic error distributions for the Euler method for stochastic differential equations," *Ann. Probab.*, vol. 26, no. 1, pp. 267–307, 1998.
[39] F. Xiao, X. Tang, and L. Wang, "An explicit fourth-order accurate FDTD method based on the staggered ADAMS-bashforth time integrator," *Microw. Opt. Technol. Lett.*, vol. 49, pp. 910–912, Apr. 2007.
[40] M. F. Fathoni and A. I. Wuryandari, "Comparison between Euler, Heun, Runge-Kutta and Adams-Bashforth-Moulton integration methods in the particle dynamic simulation," in *Proc. Int. Conf. Interact. Digit. Media*, Dec. 2015, pp. 1–7.
[41] G. Psihoyios and T. E. Simos, "Trigonometrically fitted Adams-Bashforth-Moulton methods for periodic initial value problems," *Comput. Fluid Solid Mech.*, vol. 11, pp. 2097–2100, Jun. 2003.
[42] M. Yoneyama, A. Fujii, and S. Maeda, "Chemical waves on the surface of a photosensitive monolayer," *J. Amer. Chem. Soc.*, vol. 116, no. 16, pp. 7294–7298, 1994.
[43] M. Yoneyama, A. Fujii, and S. Maeda, "Wavelength-doubled spiral fragments in photosensitive monolayers," *J. Amer. Chem. Soc.*, vol. 117, no. 31, pp. 8188–8191, 1995.
[44] L. Q. Zhou and Q. Ouyang, "Experimental studies on long-wavelength instability and spiral breakup in a reaction-diffusion system," *Phys. Rev. Lett.*, vol. 85, pp. 1650–1653, Aug. 2000.
[45] Q. Ouyang, H. L. Swinney, and G. Li, "Transition from spirals to defect-mediated turbulence driven by a Doppler instability," *Phys. Rev. Lett.*, vol. 84, pp. 1047–1050, Jan. 2000.
[46] A. Goryachev, H. Chaté, and R. Kapral, "Synchronization defects and broken symmetry in spiral waves," *Phys. Rev. Lett.*, vol. 80, pp. 873–876, Jan. 1998.
[47] D. Barkley, M. Kness, and L. S. Tuckerman, "Spiral-wave dynamics in a simple model of excitable media: The transition from simple to compound rotation," *Phys. Rev. A, Gen. Phys.*, vol. 42, pp. 2489–2492, Aug. 1990.
[48] J. J. Tyson, "Target patterns in a realistic model of the Belousov–Zhabotinskii reaction," *J. Chem. Phys.*, vol. 73, no. 5, pp. 2224–2237, 1980.
[49] J. J. Tyson and J. P. Keener, "Singular perturbation theory of traveling waves in excitable media," *Phys. D, Nonlinear Phenomena*, vol. 32, pp. 327–361, Dec. 1988.
[50] O. Kwon, T. Y. Kim, and K. J. Lee, "Period-2 spiral waves supported by nonmonotonic wave dispersion," *Phys. Rev. E, Stat. Phys. Plasmas Fluids Relat. Interdiscip. Top.*, vol. 82, Oct. 2010, Art. no. 046213.

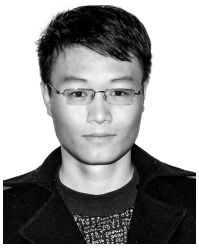

JIAN GAO received the M.S. degree in theoretical physics from Jiangsu Normal University, Xuzhou, in 2017. He is currently pursuing the Ph.D. degree with the University of Shanghai for Science and Technology.

He is the author of more than five articles. His research interests include nonlinear dynamics, pattern formation, population distribution, and chemical waves.

CHANGGUI GU received the B.S. and M.S. degrees from Yangzhou University, Yangzhou, in 2008, and the Ph.D. degree from East China Normal University, Shanghai, in 2012, all in complex networks and nonlinear science.

From 2012 to 2014, he was a Researcher with Leiden University. Since 2015, he has been an Associate Professor with the University of Shanghai for Science and Technology. He is the author of more than 50 articles. His research interests include time series analysis theory, complex network theory, and the application in complex systems, such as transportation and biology.